PHYSICAL REVIEW B **109**, 144424 (2024)

Terahertz spin-wave excitations in the transverse conical phase of $BiFeO_3$

B. Tóth,[1,*] D. G. Farkas,[1] K. Amelin,[2] T. Rõõm,[2] U. Nagel,[2] L. Udvardi,[3] L. Szunyogh,[3,4]
L. Rózsa,[5,3] T. Ito,[6] and S. Bordács[1,4,7]
[1]*Department of Physics, Institute of Physics, Budapest University of Technology and Economics,*
Műegyetem rakpart 3, H-1111 Budapest, Hungary
[2]*National Institute of Chemical Physics and Biophysics, Akadeemia tee 23, 12618 Tallinn, Estonia*
[3]*Department of Theoretical Physics, Institute of Physics, Budapest University of Technology and Economics,*
Műegyetem rakpart 3, H-1111 Budapest, Hungary
[4]*HUN-REN–BME Condensed Matter Physics Research Group, Budapest University of Technology and Economics,*
Műegyetem rakpart 3, H-1111 Budapest, Hungary
[5]*Department of Theoretical Solid State Physics, Institute for Solid State Physics and Optics,*
HUN-REN Wigner Research Centre for Physics, H-1525 Budapest, Hungary
[6]*National Institute of Advanced Industrial Science and Technology, Tsukuba, Ibaraki 305-8562, Japan*
[7]*Experimental Physics V, Center for Electronic Correlations and Magnetism,*
University of Augsburg, D-86135 Augsburg, Germany

(Received 2 February 2024; accepted 11 April 2024; published 26 April 2024; corrected 3 July 2024)

Although $BiFeO_3$ is one of the most studied multiferroic materials, recent magnetization and neutron scattering studies have revealed a new magnetic phase in this compound—the transverse conical phase. To study the collective spin excitations of this phase, we performed terahertz spectroscopy in magnetic fields up to 17 T at and above room temperature. We observed five spin-wave branches in the magnetic phase with long-wavelength conical modulation. Using a numerical spin dynamics model, we found two kinds of excitations with magnetic moments oscillating either along or perpendicular to the static fields. Remarkably, we detected strong directional dichroism, an optical manifestation of the magnetoelectric effect, for one spin-wave mode of the conical phase. According to our experiments, the stability of the conical state is sensitive to the magnetic-field history, and it can become (meta)stable at or close to zero magnetic field, which may allow exploiting its magnetoelectric properties at room temperature.

DOI: 10.1103/PhysRevB.109.144424

I. INTRODUCTION

Among magnetoelectric multiferroics, i.e., materials with coexisting ferroelectric and magnetic orders [1–4], $BiFeO_3$ attracted particular interest [5] because (1) it is one of the few room-temperature multiferroics [4], (2) it shows large ferroelectric polarization, even compared with conventional ferroelectrics [6], and (3) it has a complex magnetic structure shaped by competing interactions [7,8]. Based on the magnetoelectric (ME) coupling between the electric polarization and the magnetic order, several potential applications of multiferroics were envisaged, such as magnetoelectric memory and logic devices [9–14]. $BiFeO_3$ has been a test bed for these concepts, and many fundamental features relevant for applications, such as electric field control of magnetic domains [15] and magnetization [10] and nonreciprocal light absorption [16], have been demonstrated in this material.

Even though $BiFeO_3$ has been studied extensively, large, ferroelectric monodomain single crystals became available only in the last 10 years [17]. These laser-floating-zone-grown crystals allowed the systematic characterization of magnetic-field-induced electric polarization [18,19], observation of magnetic-field-induced reorientation of the cycloidal domains [20], determination of the optical selection rules of spin waves [21], and measurement of their anisotropy [22]. Remarkably, the magnetic-field-temperature phase diagram of $BiFeO_3$ has still not been fully explored: recently, a new magnetic phase, the transverse conical state, was discovered above 150 K [23,24]. Although the spin-wave excitations of $BiFeO_3$ have been studied close to room temperature using inelastic neutron scattering [22,25,26], Raman [27], and terahertz (THz) [16,28–31] spectroscopies, the spin-wave excitation spectrum in the transverse conical phase has remained unexplored. Here, we study the spin-wave excitations in this magnetic-field-induced transverse conical phase, but before presenting the results, we briefly summarize the most important aspects of the phase diagram of bulk $BiFeO_3$ below.

The perovskite structure of $BiFeO_3$ [see Fig. 1(a)] undergoes a lattice distortion at around 1100 K, and its symmetry decreases to the rhombohedral $R3c$ [32,33]. Upon this structural transition, ferroelectric polarization appears along one of the $\langle 111\rangle$-type body diagonals [34]. Throughout the paper, we use the Cartesian system $\{\mathbf{X}, \mathbf{Y}, \mathbf{Z}\}$ with axes parallel to $\{[1\bar{1}0], [11\bar{2}], [111]\}$, as shown in Fig. 1(a). In the rhombohedral phase, below 640 K, a cycloidally modulated antiferromagnetic order sets in [see Fig. 1(b)] [35]; thus, $BiFeO_3$ becomes multiferroic well above room temperature.

---

[*] toth.boglarka@ttk.bme.hu

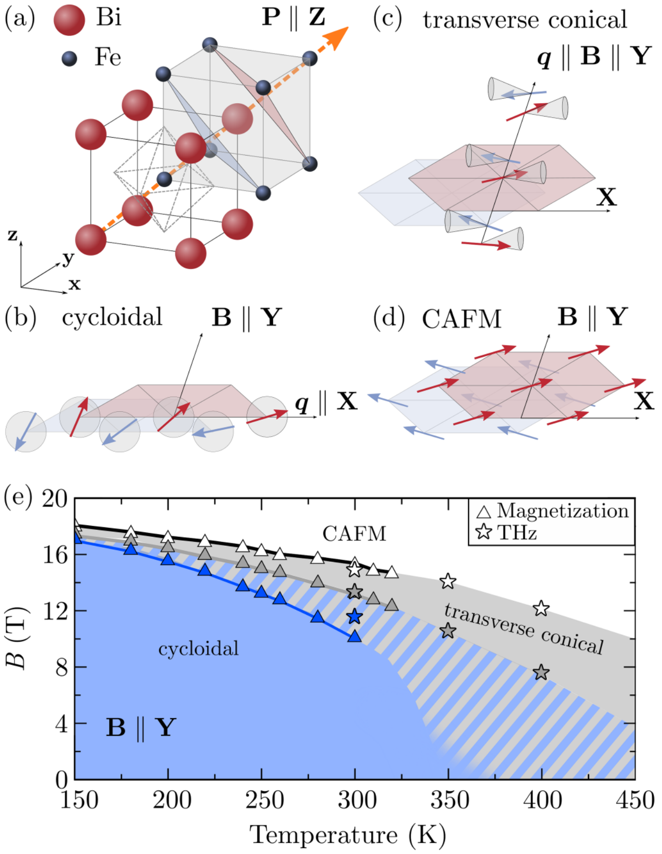

FIG. 1. (a) Perovskite unit cell of $BiFeO_3$. The $\{\mathbf{x}, \mathbf{y}, \mathbf{z}\}$ axes show the coordinate system of the pseudocubic unit cell. The $\mathbf{Z} = [111]/\sqrt{3}$ axis is parallel to the hexagonal axis, while $\mathbf{X} = [1\bar{1}0]/\sqrt{2}$ and $\mathbf{Y} = [11\bar{2}]/\sqrt{6}$ are in the perpendicular plane. At 1100 K, the unit cell undergoes a rhombohedral distortion, and electric polarization emerges along a body diagonal. (b)–(d) Schematic drawings of magnetic structures in the different phases of $BiFeO_3$ when the static field **B** points along **Y**. Spins in two antiferromagnetically coupled hexagonal planes, light red and light blue, are shown. (e) Magnetic phase diagram of $BiFeO_3$ as a function of temperature and magnetic field. In increasing fields, the cycloidal-transverse conical phase boundary is indicated by gray symbols, and the conical-canted antiferromagnetic phase boundary is indicated with white symbols. In decreasing fields, the conical-to-cycloidal transition is marked by blue symbols. The striped region shows the hysteretic region. Stars are the THz data from this work, and triangles are the magnetization data from Ref. [23].

The strongest Heisenberg interaction between neighboring spins is antiferromagnetic, favoring a *G*-type order [26,36], i.e., with the magnetic moments pointing oppositely in consecutive atomic layers stacked along the [111] direction. The polar displacement of the ions and the antiferrodistortive rotation of the oxygen octahedra allow for homogeneous and staggered Dzyaloshinskii-Moriya (DM) interactions [37]. In competition with the Heisenberg interaction, the homogeneous DM interaction leads to the cycloidal modulation of the antiferromagnetic structure. The staggered component is responsible for a local weak-ferromagnetic component appearing perpendicular to the ferroelectric polarization. As the spins of the cycloidal structure rotate, this term results in an additional spin-density wave modulation [38]. The q vectors describing the modulated order lie in the plane perpendicular to the ferroelectric polarization and parallel to one of the three equivalent $\langle 1\bar{1}0\rangle$-type (**X**-type) directions [34].

In a magnetic field applied in the XY plane, the q vectors rotate in the plane perpendicular to the field, and at low temperature, above 7 T only domains with q vectors (nearly) perpendicular to the field remain [20,21]. This rearrangement is mainly driven by the difference between the longitudinal and transverse susceptibilities defined with respect to the local antiferromagnetic order parameter. A sufficiently high magnetic field suppresses the modulated order, and a two-sublattice canted antiferromagnetic (CAFM) order with a finite weak magnetic moment along the applied field [see Fig. 1(d)] becomes energetically favorable [7,18,39,40].

At temperatures above 150 K, recent magnetization and polarization measurements [23] and neutron scattering studies [24] revealed an intermediate phase between the cycloidal and the CAFM phases see Fig. 1(e). In agreement with former theoretical predictions [41], this transverse conical state with q vectors parallel to the field emerges as a compromise: it is a combination of spiraling and homogeneous antiferromagnetic orders, as shown in Fig. 1(c). Remarkably, this magnetic-field-induced phase possesses a linear magnetoelectric effect of 210 ps/m [23], which is exceptionally large even compared to those of orthophosphates and boracites [42–44].

Spectroscopic techniques have provided valuable information on the complex magnetic structure of $BiFeO_3$ and the interactions stabilizing it. Inelastic neutron scattering experiments revealed the magnon dispersion over the Brillouin zone, from which the nearest- and next-nearest-neighbor Heisenberg interactions were deduced [26,36]. Due to the long-wavelength modulation, the magnetic Brillouin zone is much smaller, which leads to a series of excitations close to the center of the Brillouin zone [8,45]. These spin-wave excitations of the cycloidal phase were probed by high-resolution Raman and THz spectroscopy [16,21,28,46,47]. The strength of the DM interactions and the easy-axis anisotropy were determined from the resonance frequencies. Moreover, the dynamic magnetoelectric coupling gives rise to nonreciprocal directional dichroism (NDD) in $BiFeO_3$, which is the light absorption difference for counterpropagating beams [16]. However, despite these efforts, the collective excitations of the transverse conical phase have not been studied so far.

In this paper, we present the magnetic-field dependence of the THz spectra measured in ferroelectric monodomain $BiFeO_3$ samples at 300 and 350 K up to 17 T. At such high temperatures, our magnetic-field range covers all three above-mentioned phases. Besides the resonances of the cycloidal and the CAFM phases, we observed five THz active resonances in the transverse conical phase. In increasing field, three resonances disappear, and the remaining two modes continuously evolve to the resonances of the CAFM state. Remarkably, we observed strong NDD for one mode of the conical phase. Furthermore, we derived spin-model parameters which describe well the resonances of the cycloidal and CAFM phases and qualitatively capture the spin-wave modes of the conical phase near room temperature.

II. EXPERIMENTAL METHODS

Fourier-transform infrared spectroscopy was performed on high-symmetry cuts of ferroelectric monodomain single crystals of $\mathrm{BiFeO_3}$. Three pieces, large faces normal to the **X**, **Y**, and **Z** directions, were the same as used in Refs. [21,39]. Samples were large enough to cover a 3 mm diameter hole; the thickness of the samples was about 0.5 mm, and the samples were polished to a wedged shape with 2° angle. The same experimental setup as in Ref. [21] was used to study THz absorption in a magnetic field, but the Faraday and Voigt probes were modified. The sample was placed on a small copper disk with the heater and thermometer. The sample disk was thermally isolated from the rest of the probe using plastic parts. On the optical path between the sample and the 0.3 K bolometer, four radiation shields with 4 mm diameter aperture were installed. Despite these measures, the thermal heat load from the sample probe at 300 K on the bolometer using a 40 $\mathrm{cm^{-1}}$ high-cutoff filter reduced the bolometer sensitivity about 1 order of magnitude compared to the measurements at a sample temperature of 4 K.

The magnetic-field dependence of the THz transmission was measured up to 17 T in two configurations. In the Faraday configuration, the light propagation vector **k** is parallel to the external magnetic field **B**, whereas in Voigt geometry, **k** is perpendicular to **B**. Before recording the spectra at 300 and 350 K, a magnetic field of 17 T was applied at low temperatures. This created a magnetic monodomain with the cycloidal-order q vectors aligned perpendicular to the applied field. We obtained the absorption spectrum following Ref. [21]. First, we determined the field-induced absorption difference $\Delta\alpha_B$ as

$$\Delta\alpha_B = \alpha(B) - \alpha(0\,\mathrm{T}) = -\frac{1}{d}\ln\left(\frac{\mathcal{I}(B)}{\mathcal{I}(0\,\mathrm{T})}\right), \qquad (1)$$

where $\mathcal{I}(B)$ is the intensity of the transmitted light at magnetic field B and d is the sample thickness. Next, we calculated the median of $\Delta\alpha_B$ at each frequency, for all field values, which gives us the negative value of the zero-field absorption spectrum $-\Delta\alpha_0$. With this method we recovered the absorption lines in the zero-field spectrum, which shift due to the magnetic field in frequency by more than the linewidth or are absent in magnetic-field-induced phases. Finally, the zero-field spectrum was added to $\Delta\alpha_B$ to calculate $\Delta\alpha$, $\Delta\alpha = \Delta\alpha_B + \Delta\alpha_0$. We obtained directional dichroism as the absorption difference detected upon the reversal of the magnetic field instead of the light propagation vector, following earlier experiments [16].

III. EXPERIMENTAL RESULTS

A. Magnetic-field dependence of the spin waves

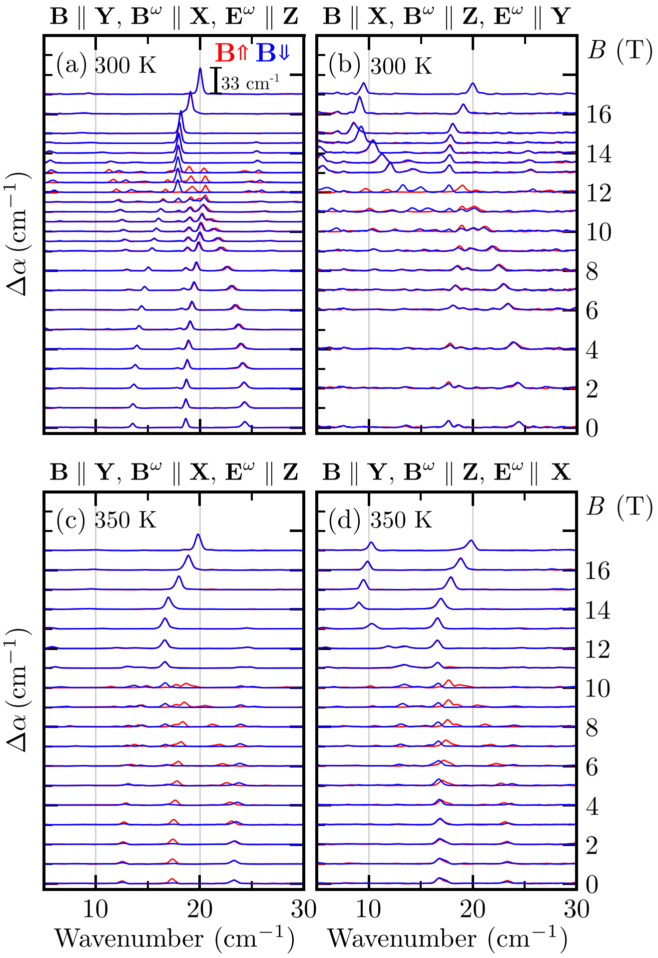

FIG. 2. (a)–(d) Magnetic-field dependence of the differential absorption spectra for various field directions and light polarizations. The spectra are shifted by a constant proportional to the magnetic-field strength. Spectra measured in increasing (decreasing) magnetic fields are red (blue). Spectra in (a) and (b) were measured at $T = 300\,\mathrm{K}$, whereas spectra in (c) and (d) were measured at $T = 350\,\mathrm{K}$.

Absorption spectra measured in the Faraday configuration at 300 and 350 K are shown in Fig. 2. Spectra recorded in increasing (decreasing) fields are plotted in red (blue). The zero-field spin-wave resonances of the cycloidal state shift to lower frequencies as the temperature is increased, in agreement with former Raman and THz spectroscopy studies [28,30,46], and follow a similar field dependence observed at low temperatures [16,21,47]. However, in higher fields, there are two pronounced anomalies in the character of the spectra corresponding to the two critical fields, B_{c1} and B_{c2}. On the border between the cycloidal and transverse conical phases, at B_{c1} the resonance frequencies suddenly change, whereas the appearance of the CAFM phase at B_{c2} is indicated by the reduction in the number of modes to two and by kinks in the magnetic-field dependence of the frequencies.

Figures 2(a) and 2(b) present THz spectra recorded at $T = 300\,\mathrm{K}$ in external fields **B** ∥ **Y** and **B** ∥ **X**, respectively. When the field is increased along **B** ∥ **Y**, B_{c1} is found between 13 and 13.5 T, and the CAFM phase is reached at $B_{c2} = 15\,\mathrm{T}$. The two strongest modes of the conical state continuously transform into the modes of the two-sublattice CAFM phase, in accordance with the second-order nature of the transition. With decreasing magnetic field, the CAFM-conical transition occurs at the same field, $B_{c2} = 15\,\mathrm{T}$, but the conical phase persists down to 12 T. When **B** ∥ **X**, the transition from the cycloidal to conical state at B_{c1} takes place between 12 and 13 T in increasing fields. The CAFM phase is reached at the same field, $B_{c2} = 15\,\mathrm{T}$, as for **B** ∥ **Y**. With decreasing field, the conical state remains stable until 12 T; then the magnetic state changes back to cycloidal. The difference in B_{c1} for $\mathbf{B} \parallel \mathbf{X}$ and $\mathbf{B} \parallel \mathbf{Y}$ detected in increasing fields may come from the in-plane magnetic anisotropy [20,21,48]. Since the cycloidal-to-conical transition at B_{c1} requires the q vector to change direction from perpendicular to parallel with the external field, the conical state for $\mathbf{B} \parallel \mathbf{X}$ has the lowest energy due to the in-plane anisotropy.

THz spectra measured at $T = 350\,\mathrm{K}$ and in field $\mathbf{B} \parallel \mathbf{Y}$ are shown in Figs. 2(c) and 2(d) for light polarizations $\mathbf{B}^{\omega} \parallel \mathbf{X}$, and $\mathbf{E}^{\omega} \parallel \mathbf{Z}$ and $\mathbf{B}^{\omega} \parallel \mathbf{Z}$ and $\mathbf{E}^{\omega} \parallel \mathbf{X}$, respectively. The critical fields at this higher temperature are lower, as expected from the phase diagram of Ref. [23]; see also Fig. 1(e) for the phase diagram based on the experimental data. The cycloidal-to-conical phase transition occurs between 10 and 11 T in increasing fields, whereas the conical-to-CAFM phase boundary is at $B_{c2} = 14\,\mathrm{T}$. In decreasing fields, there is no discontinuous change that would indicate the transition from the transverse conical to the cycloidal phase; i.e., the conical modes persist down to the lowest fields. After the application of a field, the spin-wave frequencies are the same in zero field, although the magnitude of the resonances changes. We may assume that at 350 K, the transverse conical state stays metastable after high-field treatment or the conical state is continuously deformed to the cycloidal state. The stabilization of the conical state in small or even zero fields is compelling because its large magnetoelectric effect becomes available in low fields. We note that zero-field stabilization of a high-magnetic-field phase by the broadening of a magnetic hysteresis is not unprecedented: the antiferromagnetic ground state of $\mathrm{Fe_2Mo_3O_8}$ was replaced by a metastable ferrimagnetic state after the application of a magnetic field, as reported recently [49,50].

To analyze the magnetic-field dependence of the resonance frequencies deduced at $T = 300\,\mathrm{K}$, we plot them in Figs. 3(a) and 3(b) for increasing fields applied along $\mathbf{X}$ and $\mathbf{Y}$, respectively. Each symbol refers to a specific polarization configuration, and the symbol size is proportional to the mode strength. Horizontal dashed lines mark critical fields B_{c1} and B_{c2}. We note that the field steps are not equidistant in the different polarization configurations and different field regions. For example, for $\mathbf{B} \parallel \mathbf{Y}$, $\mathbf{B}^{\omega} \parallel \mathbf{X}$, and $\mathbf{E}^{\omega} \parallel \mathbf{Z}$ [green downward triangles in Fig. 3(b)], spectra were recorded at every integer value of magnetic field between 0 and 9 T and every half tesla was measured between 9.5 and 15 T, but for $\mathbf{B} \parallel \mathbf{Y}$, $\mathbf{B}^{\omega} \parallel \mathbf{X}$, and $\mathbf{E}^{\omega} \parallel \mathbf{Y}$ [red upward triangles in Fig. 3(b)], only every fourth tesla was measured between 0 and 12 T, every half tesla was measured between 13 and 15 T, and above that, only 17 T was measured.

1. Cycloidal phase

Altogether, we observed seven modes in the cycloidal phase that we labeled following Ref. [21]. At the lowest energies, $\Phi_1^{(2)}$ gains intensity only in finite fields just like $\Phi_1^{(1)}$ at about 2 $\mathrm{cm^{-1}}$ higher phonon wavenumber. Ψ_0, $\Psi_1^{(2)}$, $\Psi_1^{(1)}$, and $\Phi_2^{(1,2)}$ are present already in zero fields at 13.4, 17.6, 18.5, and 24.3 $\mathrm{cm^{-1}}$, respectively. When $\mathbf{B} \parallel \mathbf{Y}$, the weak $\Psi_2^{(1,2)}$ mode also gains strength in finite fields, appearing at 25.4 $\mathrm{cm^{-1}}$. The selection rules of these modes are mostly in agreement with the low-temperature results of Ref. [21]. The only exception is $\Phi_1^{(1)}$, which is observed in Ref. [21] when $\mathbf{B} \parallel \mathbf{X}$, $\mathbf{B}^{\omega} \parallel \mathbf{Y}$, and $\mathbf{E}^{\omega} \parallel \mathbf{X}$ but is absent in our measurements. As this is a weak resonance gaining strength only in finite fields, it probably remains undetectable in the high-temperature experiments due to the reduced signal-to-noise ratio.

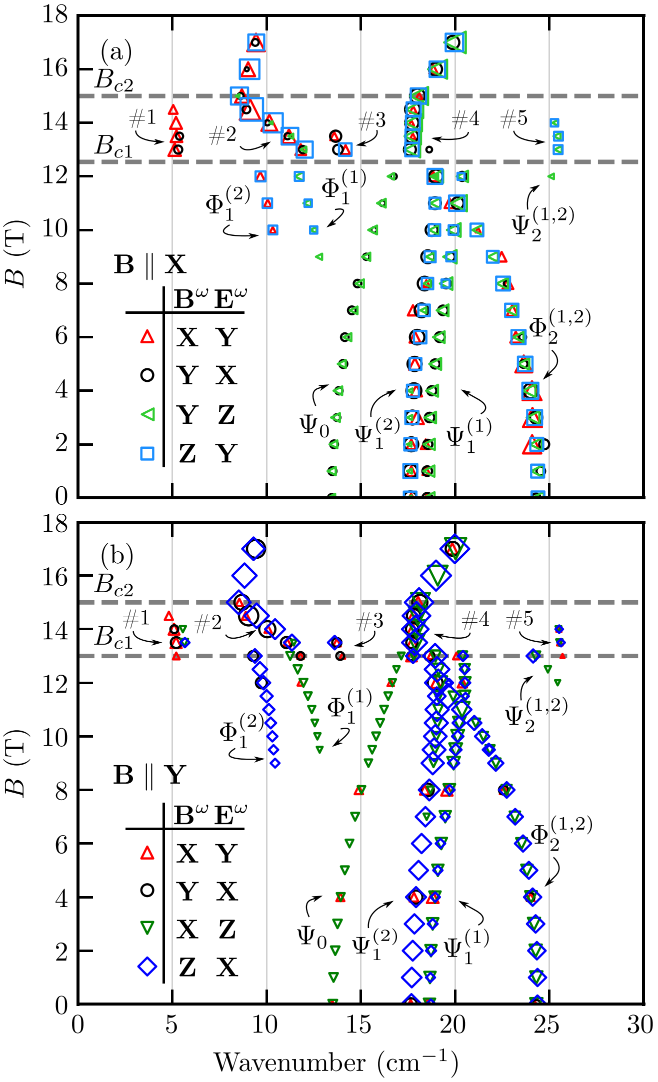

FIG. 3. Magnetic-field dependence of spin-wave frequencies and intensities at 300 K for magnetic fields (a) $\mathbf{B} \parallel \mathbf{X}$ and (b) $\mathbf{B} \parallel \mathbf{Y}$. Different symbols represent different light polarizations as given in the legends. The symbol size is proportional to the absorption line area. Gray dashed horizontal lines mark the transition fields between the cycloidal-to-conical (B_{c1}) and conical-to-CAFM (B_{c2}) phases. Φ and Ψ respectively stand for the in-plane and out-of-plane modes of the cycloidal phase.

2. Transverse conical phase

In the transverse conical phase, between B_{c1} and B_{c2}, we observe five modes (see Figs. 2 and 3). Mode 1 is at 5.5 $\mathrm{cm^{-1}}$, and mode 2 starts at 12 $\mathrm{cm^{-1}}$ and evolves into the lower-frequency mode of the CAFM phase. Mode 3 begins at 14 $\mathrm{cm^{-1}}$; mode 4, the nearly field-independent mode at 17.7 $\mathrm{cm^{-1}}$, evolves to be the higher-frequency mode of the

CAFM phase; and mode 5 emerges at 25.5 cm^{-1}. As the set of measured polarization configurations is incomplete, we can make only a few claims about the selection rules of these modes.

The two strongest modes of the conical phase, modes 2 and 4, evolve into the lower- and higher-energy modes of the CAFM phase. These resonances are present in all polarization configurations. However, mode 2 is weak for $\mathbf{B}^{\omega} \parallel \mathbf{Y}$ when $\mathbf{B} \parallel \mathbf{X}$ and also for $\mathbf{B}^{\omega} \parallel \mathbf{X}$ when $\mathbf{B} \parallel \mathbf{Y}$ [see black and green symbols in Fig. 3(a) and red and green symbols in Fig. 3(b)]. In these configurations, its strength decreases with the field, while in all other configurations, it grows as the field increases. These observations suggest that the in-plane component of $\mathbf{B}^{\omega}$ perpendicular to the static field does not significantly couple to this resonance. Mode 4 is weak for polarization $\mathbf{B}^{\omega} \parallel \mathbf{X}$ and $\mathbf{E}^{\omega} \parallel \mathbf{Y}$ for both external field directions (see red triangles in Fig. 3).

The other three modes are weaker and lose intensity with increasing fields. Mode 1, with decreasing energy and strength, is active in all configurations when $\mathbf{B} \parallel \mathbf{Y}$. Even though we observed this mode in only two polarization configurations for $\mathbf{B} \parallel \mathbf{X}$, we cannot draw further conclusions because it is close to the low-frequency cutoff of the THz spectroscopy setup. Similarly, mode 5 is close to the high-frequency cutoff set by the 40 cm^{-1} low-pass filter. For both $\mathbf{B} \parallel \mathbf{X}$ and $\mathbf{B} \parallel \mathbf{Y}$, mode 3 is silent in one polarization configuration for $\mathbf{B}^{\omega} \parallel \mathbf{Y}$ and $\mathbf{E}^{\omega} \parallel \mathbf{Z}$ and for $\mathbf{B}^{\omega} \parallel \mathbf{X}$ and $\mathbf{E}^{\omega} \parallel \mathbf{Z}$, respectively (green symbols in Fig. 3). As neither of these fields can excite this mode, it is electric dipole active only for electric fields oscillating in plane, while $\mathbf{B}^{\omega}$ along $\mathbf{Z}$ or $\mathbf{B}$ may also excite this resonance.

3. CAFM phase

In the high-field CAFM phase, two resonances emerge from the strongest modes of the conical phase. The lower-frequency mode is strong in two polarization configurations for both external field directions. When $\mathbf{B} \parallel \mathbf{X}$, those are $\mathbf{B}^{\omega} \parallel \mathbf{X}$ and $\mathbf{E}^{\omega} \parallel \mathbf{Y}$ and $\mathbf{B}^{\omega} \parallel \mathbf{Z}$ and $\mathbf{E}^{\omega} \parallel \mathbf{Y}$. And when $\mathbf{B} \parallel \mathbf{Y}$, the favored polarizations are $\mathbf{B}^{\omega} \parallel \mathbf{Y}$ and $\mathbf{E}^{\omega} \parallel \mathbf{X}$ and $\mathbf{B}^{\omega} \parallel \mathbf{Z}$ and $\mathbf{E}^{\omega} \parallel \mathbf{X}$. This lower-frequency mode is also present for $\mathbf{B} \parallel \mathbf{X}$, $\mathbf{B}^{\omega} \parallel \mathbf{Y}$, and $\mathbf{E}^{\omega} \parallel \mathbf{X}$ but is much weaker than in the former cases. Therefore, the lower-frequency mode interacts weakly with in-plane $\mathbf{B}^{\omega}$ perpendicular to $\mathbf{B}$. The higher-frequency mode is present in all configurations but is very weak when $\mathbf{B}^{\omega} \parallel \mathbf{X}$ and $\mathbf{E}^{\omega} \parallel \mathbf{Y}$ for both $\mathbf{B} \parallel \mathbf{X}$ and $\mathbf{B} \parallel \mathbf{Y}$. As can be seen from Figs. 3(a) and 3(b), the CAFM spin-wave frequencies do not depend on the magnetic-field direction in the hexagonal plane: they are the same for $\mathbf{B} \parallel \mathbf{X}$ and $\mathbf{B} \parallel \mathbf{Y}$. This is different from the case at liquid He temperatures, in which the higher-energy mode shifted to higher energy when the magnetic field direction changed from $\mathbf{B} \parallel \mathbf{X}$ to $\mathbf{B} \parallel \mathbf{Y}$ [39].

B. Directional dichroism of the spin waves

A finite-frequency manifestation of the ME effect is the so-called NDD [16,51–53]; namely, the light absorption coefficient is different for light passing through a medium in opposite directions. In $\mathrm{BiFeO_3}$, the reversal of the external magnetic field is considered to be equivalent to the reversal of the light propagation direction [16]; thus, we detected NDD as the difference in the absorption spectrum for positive and negative field directions. We measured absorption spectra for $\mathbf{k} \parallel \mathbf{Z}$ in two Voigt configurations, $\mathbf{B} \parallel \mathbf{X}$ and $\mathbf{B} \parallel \mathbf{Y}$. The results are presented in Fig. 4 for increasing field magnitudes at $T = 300$ K. The finite difference between the spectra measured in positive and negative fields is the NDD (compare red and black curves in Fig. 4). The dichroism is present in all three phases, and its magnitude is the largest in the conical phase for mode 4 close to the upper critical field, $B_{c2} \approx 15$ T.

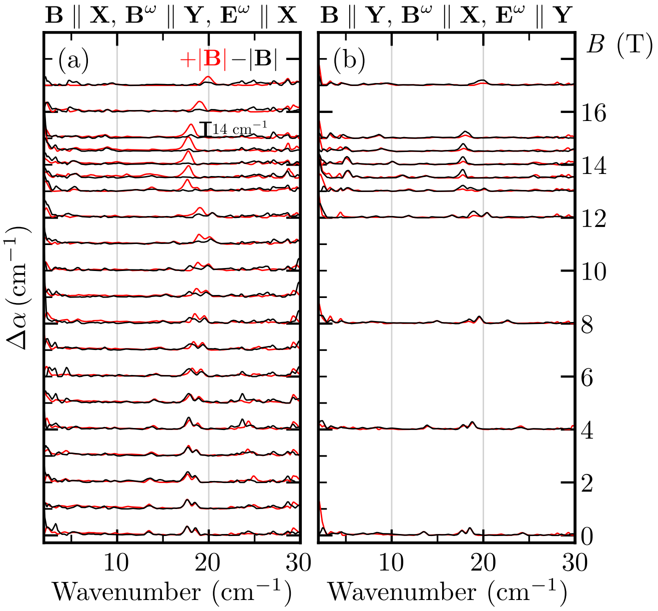

FIG. 4. Spectra measured at $T = 300$ K in positive (red) and negative (black) fields with increasing magnitude are shown for various light polarizations. The difference between the absorption measured in positive and negative fields is the nonreciprocal directional dichroism.

Studying the sum rule of NDD spectra may provide information about the static ME susceptibility [54]:

$$\chi^{\mathrm{ME}}_{\gamma\delta}(0) = \frac{c}{2\pi}\mathcal{P}\int_0^{\infty}\frac{\Delta\alpha_k(\omega)}{\omega^2}d\omega, \qquad (2)$$

where $\Delta\alpha_k(\omega) = \alpha_{+k}(\omega) - \alpha_{-k}(\omega)$ is the difference in the absorption spectra. We calculated $\Delta\alpha_k$ as the difference of the absorption spectra measured in positive and negative magnetic fields (see Fig. 4). The ω^2 dependence in Eq. (2) implies that the strongest contribution to the static ME susceptibility comes from NDD of low-frequency modes. In the present experimental configuration, when $\mathbf{B} \parallel \mathbf{X}$, $\mathbf{B}^{\omega} \parallel \mathbf{Y}$, and $\mathbf{E}^{\omega} \parallel \mathbf{X}$, the contribution of the spin waves to the ME susceptibility at 14 T is 3.3 ps/m as calculated with Eq. (2).

The static ME effect of the conical phase was studied in Ref. [23], which probed the longitudinal response χ^{ME}_{YY}, i.e., measured the magnetic-field-induced electric polarization in increasing magnetic fields. However, this experiment provided a different component of the ME tensor compared to our THz results. Here, the oscillating magnetic field $\mathbf{B}^{\omega}$ is perpendicular to the static field $\mathbf{B}$; i.e., it corresponds to

TABLE I. Exchange, DM, and anisotropy parameters used in the simulations.

	J_1 (meV)	J_2 (meV)	D_1 (μeV)	D_2 (μeV)	K (μeV)
Set 1	4.9	0	177	77.3	3.1
Set 2	4.9	0.17	177	77.3	3.1

the transverse response χ_{XY}^{ME} or χ_{YX}^{ME}, which can be measured either by rotating a static field or by adding a small oscillatory field perpendicular to the static field. Thus, our results give an estimate of the spin-wave contribution to the static ME susceptibility, which may be verified in one of these configurations.

IV. THEORETICAL MODELING OF SPIN-WAVE RESONANCES

Following the literature [8], we used the Hamiltonian below to calculate the spin-wave resonances of the various phases:

$$\begin{aligned}\mathcal{H} = {} & J_1 \sum_{\langle i,j\rangle} \mathbf{S}_i \cdot \mathbf{S}_j + J_2 \sum_{\langle i,j\rangle'} \mathbf{S}_i \cdot \mathbf{S}_j \\ & + D_1 \sum_{\langle i,j\rangle} (\mathbf{Z} \times \mathbf{e}_{ij}/a)(\mathbf{S}_i \times \mathbf{S}_j) \\ & + D_2 \sum_{\langle i,j\rangle} (-1)^{h_i} \mathbf{Z}(\mathbf{S}_i \times \mathbf{S}_j) \\ & - K \sum_i S_{iZ}^2 + g\mu_{\mathrm{B}} \sum_i \mathbf{S}_i \cdot \mathbf{B}, \end{aligned} \tag{3}$$

where a is the pseudocubic lattice constant (see Fig. 1). Each site $\mathbf{R}_i$ is occupied by an Fe atom with a classical spin vector $\mathbf{S}_i$ of length $S = 5/2$, and the nearest neighbors $\langle i, j\rangle$ are connected by the vector $\mathbf{R}_j = \mathbf{R}_i + \mathbf{e}_{ij}$. J_1 and J_2 are the exchange coupling constants between nearest and next-nearest neighbors. D_1 and D_2 are the homogeneous and staggered components of the nearest-neighbor DM interaction, respectively, and $h_i = \sqrt{3}\mathbf{R}_i \cdot \mathbf{Z}/a$ labels the hexagonal layers. The coupling constant of the easy-axis anisotropy is denoted by K. The g factor is $g = 2$, μ_{B} is the Bohr magneton, and $\mathbf{B}$ is the magnetic field. The model parameters are collected in Table I.

We performed simulations for a cell consisting of six layers along the $\mathbf{Z}$ direction, enabling the use of periodic boundary conditions when considering the three alternating in-plane atomic positions in the pseudocubic lattice along this direction and the antiferromagnetic alignment between neighboring layers. The system size was larger along the wave-vector direction, i.e., $\mathbf{X}$ perpendicular to the field direction for modeling the cycloidal structure and $\mathbf{Y}$ along the field for the conical spiral, while the size was kept minimal along the direction perpendicular to the long side. Periodic boundary conditions were used along all directions, and a single period of the spin spiral was included in the cell. The period of the spiral, i.e., the length of the long side of the cell, was optimized at each magnetic-field value by calculating the ground-state energy per spin for various cell sizes.

The energy was found by initializing a system in a harmonic spin cycloid. The energy of this state was minimized first by numerically solving the Landau-Lifshitz-Gilbert equation using the full Hamiltonian, then speeding up the relaxation close to the energy minimum by aligning the spins with the direction of the local effective magnetic field in each step. The convergence was stopped when the torque expressed in frequency units became smaller than 10^{-8} meV$g/\hbar$ at each lattice site. The spin-wave frequencies were calculated within linear spin-wave theory close to this energy minimum. The spin-wave eigenvectors of each mode n were used to determine the response function $|\chi_0^n|^2$ to a spatially homogeneous external magnetic field at the spin-wave frequency; i.e., the response function is proportional to the magnetic dipole strength of the mode. Details of the calculation method and the definition of the response function are reported in Ref. [55].

The calculated spin-wave resonances are compared with the experimental results in Fig. 5. In Fig. 5(a), excitations are calculated with parameter set 1 given in Table I. We optimized these coupling constants to fit the cycloidal wavelength λ (62 nm), the zero-field resonances of the cycloidal state, and the field dependence of the modes in the CAFM phase. In this phase, D_2 and the product J_1K determine the resonances, ω_{ν_2} and ω_{ν_1} [39], in agreement with Ref. [56]:

$$\omega_{\nu_2} = \gamma\sqrt{B^2 + BB_D}, \tag{4}$$

$$\omega_{\nu_1} = \gamma\sqrt{BB_D - 2B_EB_A + B_D^2}, \tag{5}$$

where γ is the gyromagnetic ratio and we introduced the following effective fields: $B_D = \frac{z_1 D_2 S}{g\mu_B}$, $B_E = \frac{z_1 J_1 S}{g\mu_B}$, and $B_A = \frac{2KS}{g\mu_B}$, where $z_1 = 6$ is the number of nearest neighbors. The in-plane, Φ_n, and out-of-plane, Ψ_n, excitation frequencies of the zero-field cycloidal state may be well approximated by $\omega_{\Phi_n} \approx \gamma\sqrt{B_E B_L^2/(2B_S)}n$ and $\omega_{\Psi_n} \approx \gamma\sqrt{B_E B_L^2/(2B_S)(n^2+1)}$, respectively, with $B_L = \frac{2D_1S}{g\mu_B}$ and $B_S = \frac{(J_1-4J_2)S}{g\mu_B}$ [8,45]. The non-negative integer index n labels the spin-wave modes at nQ, where $\mathbf{Q}$ is the cycloidal ordering wave vector, $Q = 2\pi/\lambda$. The ratio $2\pi(2B_S)/B_L$ is the period of the cycloid in units of a in $\mathbf{B} = 0$. The period and the frequencies are perturbed by the anisotropy in combination B_EB_A. In order to reduce the number of free parameters, first, we set $J_2 = 0$. The four parameters in set 1 describe well the magnetic-field dependence of the resonance frequencies in the cycloidal and CAFM phase, and also the lower critical field B_{c1}. Besides the frequencies, the numerical model correctly describes the motion of spins in the cycloidal phase as the modes labeled as Ψ and Φ indeed correspond to the out-of-plane and in-plane oscillations of the spins. The parameter values in set 1 are similar to, although somewhat lower than, the ones applied to describe the low-temperature resonances [16,21,39]. In these publications, the same model was used apart from a sign difference in the definition of the exchange terms in the Hamiltonian, Eq. (3). The decrease of the interaction parameters accounts for the lowered excitation frequencies in the high-temperature experiments

In the transverse conical state, the model qualitatively describes the field dependence of the resonances and gives an almost field-independent q vector in accordance with recent

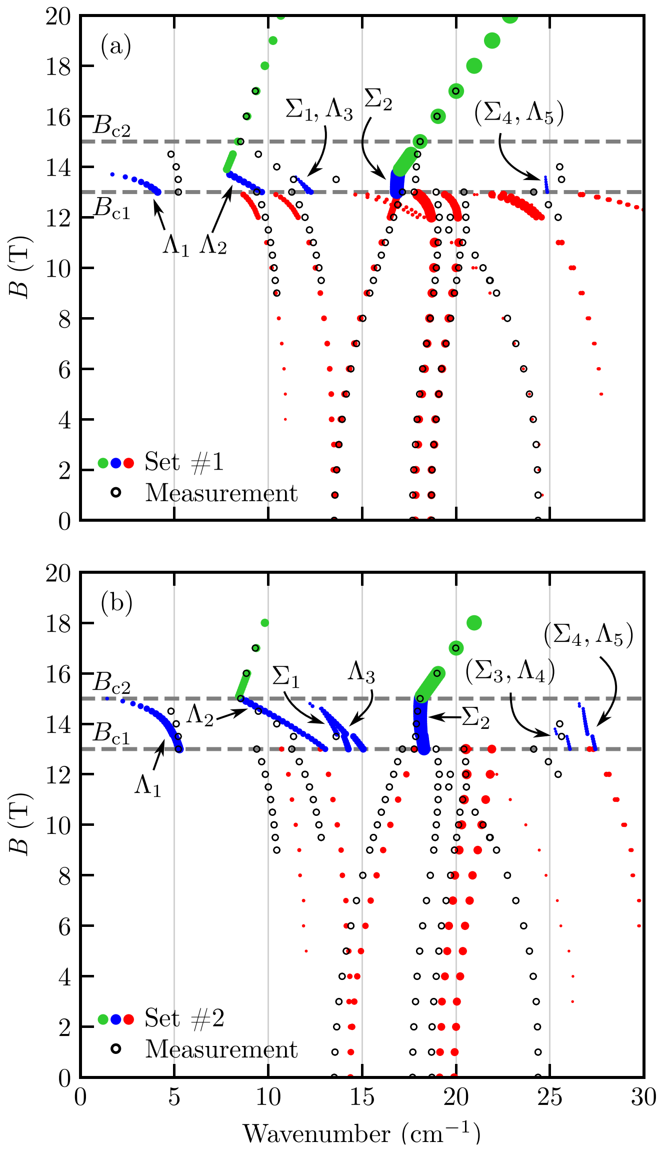

FIG. 5. The resonance positions calculated using the model Hamiltonian defined in Eq. (3) with (a) parameter set 1 and (b) parameter set 2, as given in Table I. Red, blue, and green dots show the theoretical frequencies in the cycloidal, transverse conical, and CAFM phases, respectively. The size of the dots is proportional to the magnetic dipole strength of the given mode. Λ_n and Σ_n correspond to modes with oscillating magnetic moments parallel and perpendicular to the static field, respectively. The resonance frequencies measured in experiments in external magnetic fields parallel to **Y** are shown in black. Gray dashed horizontal lines mark the transition fields between the cycloidal-conical (B_{c1}) and conical-CAFM (B_{c2}) phases in the experiments.

neutron scattering experiments [24]. The eigenmodes can be classified into two groups. They possess an oscillating magnetic moment either parallel or perpendicular to the static field; thus, we label them Λ_n and Σ_n, respectively. Λ_1, which is the lowest-energy mode of the conical phase, i.e., mode 1 in Fig. 3(a), corresponds to the opening and closing of the cone angle. As expected from this motion, it softens and loses its strength toward B_{c2}. In agreement with the experimental finding that mode 2 is not significantly coupled to an in-plane $\mathbf{B}^{\omega}$ perpendicular to $\mathbf{B}$, we assign it to Λ_2. As mode 3 shows a similar selection rule, it is likely Λ_3, although it may overlap with Σ_1, appearing at almost the same energy in the numerical calculations. Although we could not deduce clear selection rules for mode 4, it is clearly the Σ_2 mode based on the calculations. Mode 5 could be one of the pairs (Σ_3, Λ_4) and (Σ_4, Λ_5), which are almost degenerate in the calculations. The (Σ_3, Λ_4) pair is not visible in Fig. 5(a) because of its low intensity. However, experimentally, we could not distinguish between modes Σ_3, Σ_4, Λ_4, and Λ_5. Experimentally, some of the modes are active in polarizations where the magnetic dipole selection rules do not predict their appearance; these may be excited by the oscillating electric field through the strong magnetoelectric effect detected in the conical phase.

Despite the qualitative agreement between theory and experiment, calculations predict lower frequencies in the conical phase and also a lower transition field, $B_{c2} \approx 13.8$ T. The upper critical field may be found as the field below which the CAFM phase becomes unstable against periodic modulations, i.e., the energy of a finite-q spin-wave becomes negative [57]. The equation derived can be formally expressed with the frequencies of the modes in the CAFM phase at B_{c2} and the zero-field cycloidal frequency ω_{Ψ_0}:

$$\omega_{\nu_2}(B_{c2}) + \omega_{\nu_1}(B_{c2}) = 2\omega_{\Psi_0}. \tag{6}$$

Therefore, once the spin-wave frequencies in the zero-field cycloidal state and in the CAFM phase are fixed, B_{c2} cannot be modified by tuning the parameters. By introducing a finite J_2 in the original parameter set (see set 2 in Table I) the stability range of the modulated phases is extended, and the CAFM phase appears above $B_{c2} \approx 15$ T, as shown in Fig. 5(b). However, the energy of the conical phase is lower than that of the cycloidal phase only in a narrow field range above $B_{c1} = 14.9$ T. Although the conical state is not a global energy minimum below B_{c1}, it remains a local minimum, allowing us to calculate excitations above this metastable state. In Fig. 5(b), we show the spin-wave resonances of the conical state in the 13–15 T field range. The correspondence between theory and experiment becomes much better in the conical phase as the modes are shifted to higher frequencies. However, increasing J_2 leads to smaller exchange stiffness and thus a longer cycloidal q vector and correspondingly increased spin-wave frequencies in the cycloidal phase.

We could not find a parameter set that captures the critical fields and the resonance frequencies in all three phases. The sizable magnetostriction observed across the magnetic phase transition [23] may explain why a single field-independent parameter set cannot describe all the experimental results. At low temperatures, the introduction of additional anisotropy parameters induced by magnetostriction explained the anisotropy of the resonances detected in the CAFM phase [39]. However, at high temperatures the magnetic resonances of the CAFM phase are not sensitive to the in-plane rotation of the field as seen in Fig. 3. Moreover, the introduction of such additional anisotropies can modify the frequencies in the CAFM phase, but Eq. (6) remains valid. This means that additional anisotropies cannot change the upper critical field B_{c2} if the resonance frequencies are fixed. When fixing ω_{ν_2}, ω_{ν_1}, and B_{c2}, we could only take into account the magnetostriction by considering a different value of $\omega^2_{\Psi_0} = \gamma^2 B_E B_L^2/(2B_S)$ in the cycloidal state and the CAFM phase. This coefficient is determined by parameters influencing the spatial variation of the structure, such as the exchange J_2 selected in parameter set 2 or DM interactions, but is not significantly influenced by local anisotropy terms. Since we lack sufficient data to determine how all of the model parameters change as a consequence of the magnetostriction, we propose a minimal model in which considering two different values of J_2 is sufficient to quantitatively describe the spin-wave frequencies in all three phases and the two critical fields.

V. SUMMARY

We studied the spin-wave excitations of the transverse conical state of $BiFeO_3$ by THz spectroscopy. We determined the magnetic-field dependence of spin-wave excitations in all three phases at room temperature and above: the cycloidal, transverse conical, and CAFM phases. Moreover, we analyzed selection rules for the linearly-polarized THz radiation absorption spectra. In the transverse conical phase we observed five modes, among which two evolve into the resonances of the CAFM phase. As a manifestation of the magnetoelectric effect, we also observed nonreciprocal directional dichroism, which is the strongest in the conical state. We developed a numerical model that describes well the resonances of the cycloidal and CAFM phases. The agreement between theory and experiment is qualitative in the conical phase, indicating the importance of magnetostriction. Based on this model, we classified the resonances of the conical state into two groups: active for magnetic moments oscillating either along or perpendicular to the static field. Finally, we found that the conical state, which shows a strong linear magnetoelectric effect and directional dichroism, may become (meta)stable at or close to zero magnetic field. Given the strain tunability of the magnetic phases in $BiFeO_3$ [58–60], thin-film technology may allow the realization of these peculiar effects at room temperature.

ACKNOWLEDGMENTS

We thank R.S. Fishman for discussions. The authors acknowledge the support of the bilateral program of the Estonian and Hungarian Academies of Sciences under Contracts No. NKM 2018-47, No. NKM 2021-24, and No. NKM2022-27/2023. We acknowledge support from Estonian Research Council Grant No. PRG736 and European Regional Development Fund Project No. TK134. This research was supported by the Ministry of Culture and Innovation and the National Research, Development and Innovation Office within the Quantum Information National Laboratory of Hungary (Grant No. 2022-2.1.1-NL-2022-00004). This work was supported by the Hungarian National Research, Development and Innovation Office (NKFIH Grants No. FK 135003, No. K 131938, No. K 142652, and No. FK 142601), as well as by the Hungarian Academy of Sciences via a János Bolyai Research Grant (Grant No. BO/00178/23/11).

[1] H. Schmid, Multi-ferroic magnetoelectrics, Ferroelectrics **162**, 317 (1994).

[2] N. A. Hill, Why are there so few magnetic ferroelectrics? J. Phys. Chem. B **104**, 6694 (2000).

[3] T. Kimura, T. Goto, H. Shintani, K. Ishizaka, T. Arima, and Y. Tokura, Magnetic control of ferroelectric polarization, Nature (London) **426**, 55 (2003).

[4] M. Fiebig, T. Lottermoser, D. Meier, and M. Trassin, Publisher correction: The evolution of multiferroics, Nat. Rev. Mater. **4**, 146 (2019).

[5] J.-G. Park, M. D. Le, J. Jeong, and S. Lee, Structure and spin dynamics of multiferroic $BiFeO_3$, J. Phys.: Condens. Matter **26**, 433202 (2014).

[6] J. Wang, J. B. Neaton, H. Zheng, V. Nagarajan, S. B. Ogale, B. Liu, D. Viehland, V. Vaithyanathan, D. G. Schlom, U. V. Waghmare, N. A. Spaldin, K. M. Rabe, M. Wuttig, and R. Ramesh, Epitaxial $BiFeO_3$ multiferroic thin film heterostructures, Science **299**, 1719 (2003).

[7] Y. F. Popov, A. M. Kadomtseva, G. P. Vorob'ev, and A. K. Zvezdin, Discovery of the linear magnetoelectric effect in magnetic ferroelectric $BiFeO_3$ in a strong magnetic field, Ferroelectrics **162**, 135 (1994).

[8] R. S. Fishman, Field dependence of the spin state and spectroscopic modes of multiferroic $BiFeO_3$, Phys. Rev. B **87**, 224419 (2013).

[9] M. Bibes and A. Barthélémy, Towards a magnetoelectric memory, Nat. Mater. **7**, 425 (2008).

[10] Y.-H. Chu, L. W. Martin, M. B. Holcomb, M. Gajek, S.-J. Han, Q. He, N. Balke, C.-H. Yang, D. Lee, W. Hu, Q. Zhan, P.-L. Yang, A. Fraile-Rodríguez, A. Scholl, S. X. Wang, and R. Ramesh, Electric-field control of local ferromagnetism using a magnetoelectric multiferroic, Nat. Mater. **7**, 478 (2008).

[11] J. T. Heron, J. L. Bosse, Q. He, Y. Gao, M. Trassin, L. Ye, J. D. Clarkson, C. Wang, J. Liu, S. Salahuddin, D. C. Ralph, D. G. Schlom, J. Íñiguez, B. D. Huey, and R. Ramesh, Deterministic switching of ferromagnetism at room temperature using an electric field, Nature (London) **516**, 370 (2014).

[12] S. Manipatruni, D. E. Nikonov, C.-C. Lin, T. A. Gosavi, H. Liu, B. Prasad, Y.-L. Huang, E. Bonturim, R. Ramesh, and I. A. Young, Scalable energy-efficient magnetoelectric spin–orbit logic, Nature (London) **565**, 35 (2019).

[13] R. Ramesh, S. Manipatruni, and I. Young, Electric-field control of magnetism, MRS Bull. **44**, 288 (2019).

[14] N. A. Spaldin and R. Ramesh, Advances in magnetoelectric multiferroics, Nat. Mater. **18**, 203 (2019).

[15] T. Zhao, A. Scholl, F. Zavaliche, K. Lee, M. Barry, A. Doran, M. P. Cruz, Y. H. Chu, C. Ederer, N. A. Spaldin, R. R. Das, D. M. Kim, S. H. Baek, C. B. Eom, and R. Ramesh, Electrical control of antiferromagnetic domains in multiferroic $BiFeO_3$ films at room temperature, Nat. Mater. **5**, 823 (2006).

[16] I. Kézsmárki, U. Nagel, S. Bordács, R. S. Fishman, J. H. Lee, H. T. Yi, S.-W. Cheong, and T. Rõõm, Optical diode effect at spin-wave excitations of the room-temperature multiferroic $BiFeO_3$, Phys. Rev. Lett. **115**, 127203 (2015).

[17] T. Ito, T. Ushiyama, Y. Yanagisawa, R. Kumai, and Y. Tomioka, Growth of highly insulating bulk single crystals of multiferroic $BiFeO_3$ and their inherent internal strains in the domain-switching process, Cryst. Growth Des. **11**, 5139 (2011).

[18] M. Tokunaga, M. Akaki, T. Ito, S. Miyahara, A. Miyake, H. Kuwahara, and N. Furukawa, Magnetic control of transverse electric polarization in $BiFeO_3$, Nat. Commun. **6**, 5878 (2015).

[19] S. Kawachi, S. Miyahara, T. Ito, A. Miyake, N. Furukawa, J. I. Yamaura, and M. Tokunaga, Direct coupling of ferromagnetic moment and ferroelectric polarization in $BiFeO_3$, Phys. Rev. B **100**, 140412(R) (2019).

[20] S. Bordács, D. G. Farkas, J. S. White, R. Cubitt, L. DeBeer-Schmitt, T. Ito, and I. Kézsmárki, Magnetic field control of cycloidal domains and electric polarization in multiferroic $BiFeO_3$, Phys. Rev. Lett. **120**, 147203 (2018).

[21] D. G. Farkas, D. Szaller, I. Kézsmárki, U. Nagel, T. Rõõm, L. Peedu, J. Viirok, J. S. White, R. Cubitt, T. Ito, R. S. Fishman, and S. Bordács, Selection rules and dynamic magnetoelectric effect of the spin waves in multiferroic $BiFeO_3$, Phys. Rev. B **104**, 174429 (2021).

[22] D. Zhang, S. Dissanayake, B. Winn, M. Matsuda, T. Ito, and R. Fishman, Anisotropic spin-wave excitations in multiferroic $BiFeO_3$, Phys. Rev. B **105**, 144426 (2022).

[23] S. Kawachi, A. Miyake, T. Ito, S. E. Dissanayake, M. Matsuda, W. Ratcliff, Z. Xu, Y. Zhao, S. Miyahara, N. Furukawa, and M. Tokunaga, Successive field-induced transitions in $BiFeO_3$ around room temperature, Phys. Rev. Mater. **1**, 024408 (2017).

[24] M. Matsuda, S. E. Dissanayake, T. Hong, Y. Ozaki, T. Ito, M. Tokunaga, X. Z. Liu, M. Bartkowiak, and O. Prokhnenko, Magnetic field induced antiferromagnetic cone structure in multiferroic $BiFeO_3$, Phys. Rev. Mater. **4**, 034412 (2020).

[25] Z. Xu, J. Wen, T. Berlijn, P. M. Gehring, C. Stock, M. B. Stone, W. Ku, G. Gu, S. M. Shapiro, R. J. Birgeneau, and G. Xu, Thermal evolution of the full three-dimensional magnetic excitations in the multiferroic $BiFeO_3$, Phys. Rev. B **86**, 174419 (2012).

[26] M. Matsuda, R. S. Fishman, T. Hong, C. H. Lee, T. Ushiyama, Y. Yanagisawa, Y. Tomioka, and T. Ito, Magnetic dispersion and anisotropy in multiferroic $BiFeO_3$, Phys. Rev. Lett. **109**, 067205 (2012).

[27] P. Rovillain, M. Cazayous, Y. Gallais, A. Sacuto, R. P. S. M. Lobo, D. Lebeugle, and D. Colson, Polar phonons and spin excitations coupling in multiferroic $BiFeO_3$ crystals, Phys. Rev. B **79**, 180411(R) (2009).

[28] D. Talbayev, S. A. Trugman, S. Lee, H. T. Yi, S.-W. Cheong, and A. J. Taylor, Long-wavelength magnetic and magnetoelectric excitations in the ferroelectric antiferromagnet $BiFeO_3$, Phys. Rev. B **83**, 094403 (2011).

[29] E. Matsubara, T. Mochizuki, M. Nagai, and M. Ashida, Self-polarized terahertz magnon absorption in a single crystal of $BiFeO_3$, Phys. Rev. B **94**, 054426 (2016).

[30] M. Białek, T. Ito, H. Rønnow, and J.-P. Ansermet, Terahertz-optical properties of a bismuth ferrite single crystal, Phys. Rev. B **99**, 064429 (2019).

[31] F. Liu, Z. Jin, X. Liu, Y. Fan, J. Guo, Y. Peng, Z. Cheng, G. Ma, and Y. Zhu, Temperature dependent terahertz giant anisotropy and cycloidal spin wave modes in $BiFeO_3$ single crystal, Chin. Phys. B **29**, 077804 (2020).

[32] J. Moreau, C. Michel, R. Gerson, and W. James, Ferroelectric $BiFeO_3$X-ray and neutron diffraction study, J. Phys. Chem. Solids **32**, 1315 (1971).

[33] F. Kubel and H. Schmid, Structure of a ferroelectric and ferroelastic monodomain crystal of the perovskite $BiFeO_3$, Acta Crystallogr. Sect. B **46**, 698 (1990).

[34] I. Sosnowska, T. P. Neumaier, and E. Steichele, Spiral magnetic ordering in bismuth ferrite, J. Phys. C **15**, 4835 (1982).

[35] S. V. Kiselev, R. P. Ozerov, and G. S. Zhdanov, Detection of magnetic order in ferroelectric $BiFeO_3$ by neutron diffraction, Sov. Phys. Dokl. **7**, 742 (1963).

[36] J. Jeong, E. A. Goremychkin, T. Guidi, K. Nakajima, G. S. Jeon, S.-A. Kim, S. Furukawa, Y. B. Kim, S. Lee, V. Kiryukhin, S.-W. Cheong, and J.-G. Park, Spin wave measurements over the full Brillouin zone of multiferroic $BiFeO_3$, Phys. Rev. Lett. **108**, 077202 (2012).

[37] C. Ederer and N. A. Spaldin, Weak ferromagnetism and magnetoelectric coupling in bismuth ferrite, Phys. Rev. B **71**, 060401(R) (2005).

[38] M. Ramazanoglu, M. Laver, W. Ratcliff, S. M. Watson, W. C. Chen, A. Jackson, K. Kothapalli, S. Lee, S. W. Cheong, and V. Kiryukhin, Local weak ferromagnetism in single-crystalline ferroelectric $BiFeO_3$, Phys. Rev. Lett. **107**, 207206 (2011).

[39] T. Rõõm, J. Viirok, L. Peedu, U. Nagel, D. G. Farkas, D. Szaller, V. Kocsis, S. Bordács, I. Kézsmárki, D. L. Kamenskyi, H. Engelkamp, M. Ozerov, D. Smirnov, J. Krzystek, K. Thirunavukkuarasu, Y. Ozaki, Y. Tomioka, T. Ito, T. Datta, and R. S. Fishman, Magnetoelastic distortion of multiferroic $BiFeO_3$ in the canted antiferromagnetic state, Phys. Rev. B **102**, 214410 (2020).

[40] B. Ruette, S. Zvyagin, A. P. Pyatakov, A. Bush, J. F. Li, V. I. Belotelov, A. K. Zvezdin, and D. Viehland, Magnetic-field-induced phase transition in $BiFeO_3$ observed by high-field electron spin resonance: Cycloidal to homogeneous spin order, Phys. Rev. B **69**, 064114 (2004).

[41] Z. V. Gareeva, A. F. Popkov, S. V. Soloviov, and A. K. Zvezdin, Field-induced phase transitions and phase diagrams in $BiFeO_3$-like multiferroics, Phys. Rev. B **87**, 214413 (2013).

[42] D. N. Astrov, The magnetoelectric effect in antiferromagnetics, J. Exp. Theor. Phys. **38**, 984 (1960) [Sov. Phys. JETP **11**, 708 (1960)].

[43] M. Kumar, J.-P. Rivera, Z.-G. Ye, S. Gentil, and H. Schmid, Magnetoelectric effect in Co-Cl boracite, Ferroelectrics **204**, 57 (1997).

[44] J.-P. Rivera and H. Schmid, Search for the piezomagnetoelectric effect in $LiCoPO_4$, Ferroelectrics **161**, 91 (1994).

[45] R. de Sousa and J. E. Moore, Optical coupling to spin waves in the cycloidal multiferroic $BiFeO_3$, Phys. Rev. B **77**, 012406 (2008).

[46] M. Cazayous, Y. Gallais, A. Sacuto, R. de Sousa, D. Lebeugle, and D. Colson, Possible observation of cycloidal electromagnons in $BiFeO_3$, Phys. Rev. Lett. **101**, 037601 (2008).

[47] U. Nagel, R. S. Fishman, T. Katuwal, H. Engelkamp, D. Talbayev, H. T. Yi, S.-W. Cheong, and T. Rõõm, Terahertz spectroscopy of spin waves in multiferroic $BiFeO_3$ in high magnetic fields, Phys. Rev. Lett. **110**, 257201 (2013).

[48] R. S. Fishman, Pinning, rotation, and metastability of $BiFeO_3$ cycloidal domains in a magnetic field, Phys. Rev. B **97**, 014405 (2018).

[49] K. Matsuura, Y. Nishizawa, Y. Kinoshita, T. Kurumaji, A. Miyake, H. Oike, M. Tokunaga, Y. Tokura, and F. Kagawa, Low-temperature hysteresis broadening emerging from domain-wall creep dynamics in a two-phase competing system, Commun. Mater. **4**, 71 (2023).

[50] S. Ghara, E. Barts, K. Vasin, D. Kamenskyi, L. Prodan, V. Tsurkan, I. Kézsmárki, M. Mostovoy, and J. Deisenhofer, Magnetization reversal through an antiferromagnetic state, Nat. Commun. **14**, 5174 (2023).

[51] Y. Tokura, Multiferroics—toward strong coupling between magnetization and polarization in a solid, J. Magn. Magn. Mater. **310**, 1145 (2007).

[52] I. Kézsmárki, N. Kida, H. Murakawa, S. Bordács, Y. Onose, and Y. Tokura, Enhanced directional dichroism of terahertz light in resonance with magnetic excitations of the multiferroic Ba_2CoGeO_7 oxide compound, Phys. Rev. Lett. **106**, 057403 (2011).

[53] S. Bordács, I. Kézsmárki, D. Szaller, L. Demkó, N. Kida, H. Murakawa, Y. Onose, R. Shimano, T. Rõõm, U. Nagel, S. Miyahara, N. Furukawa, and Y. Tokura, Chirality of matter shows up via spin excitations, Nat. Phys. **8**, 734 (2012).

[54] D. Szaller, S. Bordács, V. Kocsis, T. Rõõm, U. Nagel, and I. Kézsmárki, Effect of spin excitations with simultaneous magnetic- and electric-dipole character on the static magnetoelectric properties of multiferroic materials, Phys. Rev. B **89**, 184419 (2014).

[55] L. Rózsa, M. Weißenhofer, and U. Nowak, Spin waves in skyrmionic structures with various topological charges, J. Phys.: Condens. Matter **33**, 054001 (2020).

[56] P. Pincus, Theory of magnetic resonance in αFe_2O_3, Phys. Rev. Lett. **5**, 13 (1960).

[57] N. E. Kulagin, A. F. Popkov, and A. K. Zvezdin, Spatially modulated antiferromagnetic structures in an easy-plane multiferroic, Phys. Solid State **53**, 970 (2011).

[58] D. Sando, A. Agbelele, D. Rahmedov, J. Liu, P. Rovillain, C. Toulouse, I. C. Infante, A. P. Pyatakov, S. Fusil, E. Jacquet, C. Carrétéro, C. Deranlot, S. Lisenkov, D. Wang, J.-M. Le Breton, M. Cazayous, A. Sacuto, J. Juraszek, A. K. Zvezdin, L. Bellaiche, B. Dkhil, A. Barthélémy, and M. Bibes, Crafting the magnonic and spintronic response of $BiFeO_3$ films by epitaxial strain, Nat. Mater. **12**, 641 (2013).

[59] D. Sando, A. Barthélémy, and M. Bibes, $BiFeO_3$ epitaxial thin films and devices: Past, present and future, J. Phys.: Condens. Matter **26**, 473201 (2014).

[60] P. Hemme, J.-C. Philippe, A. Medeiros, A. Alekhin, S. Houver, Y. Gallais, A. Sacuto, A. Forget, D. Colson, S. Mantri, B. Xu, L. Bellaiche, and M. Cazayous, Tuning the multiferroic properties of $BiFeO_3$ under uniaxial strain, Phys. Rev. Lett. **131**, 116801 (2023).

Correction: The second paragraph in Sec. III B, which consisted of a duplicate sentence, has been removed.